Reversible phase transformation and comprehensive phase diagram in $SrCoO_{2.5+x}$ ($0 \leqslant x \leqslant 0.5$) with the electric field control of oxygen content

Bin Lei,[1,*] Shihao Liu,[1,*] Donghui Ma,[1] Weizhuang Zhuo,[1] Wenxiang Wang,[1] Chuanqiang Wu,[2] Binghui Ge,[2] Jianjun Ying,[1] Ziji Xiang,[1] Tao Wu,[1] Zhenyu Wang,[1] and Xianhui Chen[1,3,†]

[1]*Department of Physics, and CAS Key Laboratory of Strongly-Coupled Quantum Matter Physics, University of Science and Technology of China, Hefei, Anhui 230026, China*

[2]*Information Materials and Intelligent Sensing Laboratory of Anhui Province, Key Laboratory of Structure and Functional Regulation of Hybrid Materials of Ministry of Education, Institutes of Physical Science and Information Technology, Anhui University, Hefei, Anhui 230601, China*

[3]*CAS Center for Excellence in Quantum Information and Quantum Physics, Hefei, Anhui 230026, China; CAS Center for Excellence in Superconducting Electronics (CENSE), Shanghai 200050, China; and Collaborative Innovation Center of Advanced Microstructures, Nanjing University, Nanjing, Jiangsu 210093, China*

(Received 29 June 2022; revised 28 March 2023; accepted 30 March 2023; published 10 April 2023)

Oxygen deficiency plays an essential role in tailoring the intriguing physical properties of complex oxides that can be harnessed in the cutting-edge energy and information technologies. A fine and continuous control of the oxygen content to modulate the rich physical properties of the complex oxides is highly desirable for both basic research and modern electronic technologies. Here, we report a recently developed ionic field-effect transistor (iFET) device with a solid oxygen ionic conductor (OIC) as the gate dielectric to finely and continuously control the oxygen content of the oxides. We realize a reversible structural transformation between brownmillerite $SrCoO_{2.5}$ and perovskite $SrCoO_3$ by driving oxygen ions in and out of the samples with the OICFET at room temperature. With continuously changing the oxygen content, a comprehensive phase diagram of the $SrCoO_{2.5+x}$ ($0 \leqslant x \leqslant 0.5$) thin film from an antiferromagnetic insulator to a ferromagnetic metal is obtained in a single device. Our work provides a promising route to continuously and reversibly regulate the oxygen content and to explore unique physical states in the correlated electron oxides, and represents an important step towards the realization of a long-standing goal to develop complex oxide based devices that can be integrated with existing technologies.

DOI: 10.1103/PhysRevMaterials.7.044002

I. INTRODUCTION

Correlated electron oxides exhibit a large variety of interesting phenomena, such as high-temperature superconductivity, colossal magnetoresistance, ferroelectric polarization, and metal-insulator transitions [1–5], making them attractive for applications that range from energy conversion to storage devices. In these oxide materials, oxygen defects are of particular interest as they provide a key to tailor the physical properties and to enable extended functionalities of these systems [6]. In cuprates, high-temperature superconductivity can be realized in $La_2CuO_{4+\delta}$ [7] and $YBa_2Cu_3O_{6+\delta}$ [8] from the antiferromagnetic Mott insulating state just by regulating the oxygen content (δ). Due to the close competing interactions among lattice, charge, orbital, and spin degrees of freedom in the correlated electron oxides, a small change of oxygen content often leads to profound changes in the electronic and magnetic properties. Traditional approaches to tune the oxygen content of oxide materials are primarily based on chemical oxidation or reduction, thermal annealing (in oxygen-rich atmosphere or vacuum), and so on [9–14]. In general, these methods cannot tune the oxygen concentration continuously, and are sensitive to surrounding atmosphere and cannot be integrated in electrical devices.

Pioneering efforts have been made with a liquid-gating field-effect transistor (FET) using ionic liquids (ILs) as the gate dielectric to regulate the oxygen content in oxides [15–17]. However, there still are several issues that need to be improved. First, in those IL FET devices, oxygen ions are produced through water electrolysis and enter the sample by diffusion, which lacks precise control. Second, the surfaces of samples are masked by liquid or polymer electrolytes, which is incompatible with other electronic devices and inconvenient for surface characterization and heterostructure/interface engineering. Third, the electrochemical reaction occurring at the electrolyte-solid interface may change or even damage the sample, especially at room temperature or above, which limits the tuning ability. Up to the present, some solid state electrolytes have also been used to tune the oxygen content in oxides [14,18–21]. However, the elevated operation temperature, environmental dependence, or porous/amorphous structure limits their application. Hence, a continuous and reversible oxygen-modulation ability using a field-effect transistor that is practical, compatible, and

*These authors contributed equally to this work.
†chenxh@ustc.edu.cn

integratable with modern electronic technology is much in demand.

Recently, $SrCoO_{2.5+x}$ $(0 \leqslant x \leqslant 0.5)$ (SCO) has attracted increasing research interest, because its physical properties exhibit strong oxygen content dependence. $SrCoO_{2.5}$ with an oxygen vacancy ordered brownmillerite (BMSCO) structure is an antiferromagnetic insulator, whereas $SrCoO_3$ with a simple perovskite structure (PSCO) is a ferromagnetic metal. Due to the very low formation energy and strong fluidity of oxygen vacancies in SCO, it is easy to achieve phase switching by controlling oxygen stoichiometry. Most of these studies focus on controlling the phase transformation between $SrCoO_{2.5}$ and $SrCoO_3$ by chemical oxidation or reduction [9], thermal annealing [11–13], electrochemical redox reactions [14], ionic liquid gating [16,17], and solid state electrolyte gating [19,20]. As mentioned above, these methods are more or less limited and have poor applications. Additionally, many studies focus on two ends of the phase transition, and pay little attention to the intermediate process. Hence, it is necessary to explore a different approach to track the evolution of the electronic, magnetic, and structural properties during the process of brownmillerite-perovskite transition in the SCO system.

In this work, we develop an alternative type of ionic field-effect transistor device with a solid oxygen ionic conductor (OIC), Gd-doped CeO_2 (GCO), as the gate dielectric, to manipulate the physical properties of $SrCoO_{2.5+x}$ $(0 \leqslant x \leqslant 0.5)$. Compared to those previously reported tuning approaches, the OICFET device shows reversible, continuous, and fine oxygen-modulation ability at room temperature. We achieve a reversible phase transformation between brownmillerite $SrCoO_{2.5}$ and perovskite $SrCoO_3$ by the electric-field control of oxygen migration and track the evolution of the electronic, magnetic, and structural properties during the gating process. Furthermore, a comprehensive phase diagram of the $SrCoO_{2.5+x}$ $(0 \leqslant x \leqslant 0.5)$ thin film from an antiferromagnetic insulator to a ferromagnetic metal with continuously changing the oxygen content in a single device is obtained.

II. EXPERIMENTAL METHODS

Gd-doped CeO_2 ($Ce_{0.8}Gd_{0.2}O_{1.9}$) thin films were deposited on the $(00l)$-oriented Nb-doped $SrTiO_3$ (NSTO) substrate by RF magnetron sputtering, using a sintered 20% Gd-doped CeO_2 ceramic target with 99.9% purity prepared by the sol-gel technique. The diameter of the targets is 60 mm. The substrate was cleaned by oxygen plasma in advance. Generally, the size of the substrate is $5 \times 5\,mm^2$. The RF magnetron sputtering system has a rotating substrate holder for compositional uniformity. The substrate-to-target distance is about 90 mm. During the deposition process, the RF power was fixed at 60 W. The total pressure was kept at 1.2 Pa, and the gas flow ratio of argon to oxygen was 3:1. The substrate temperature was maintained at 973 K. The growth rate is about 0.65 nm/min. In general, the thickness of the film was controlled between 400 and 800 nm. After deposition, films were *in situ* annealed at 973 K for 2 h in a 20 Pa O_2 atmosphere.

$SrCoO_{2.5}$ thin films were epitaxially grown on the $(00l)$-oriented Gd-doped CeO_2 thin film by RF magnetron sputtering, using a sintered ceramic target with 99.9% purity. The diameter of the targets was 60 mm. The substrate-to-target distance was about 50 mm. During the deposition process, the RF power was fixed at 50 W. The total pressure was kept at 12 Pa, and the gas flow ratio of argon to oxygen was 9:1. The substrate temperature was maintained at 1023 K. The growth rate is about 1.3 nm/min. In general, the growth time was about 15 min and the film thickness was ∼20 nm. After deposition, the films were cooled down to room temperature.

As-grown $SrCoO_{2.5}$ thin films were etched by argon ions in a sputtering system integrated with an argon ion etching system, leaving only an area of $75 \times 50\,\mu m^2$ previously covered with photoresist by the standard UV lithography process for the device fabrication. In order to reduce the leakage current in the gating process, a 50 nm silicon dioxide film was directly deposited on the surface of a Gd-doped CeO_2 film (except for the area where the $SrCoO_{2.5}$ film exists) in this sputtering system to isolate the electrodes from the oxygen-ion-conductor film. After removing the photoresist, electrodes were made by depositing 5 nm Cr and 50 nm Au through stencil shadow masks previously aligned on the sample in a thermal evaporation system. A back gate electrode was fabricated on the opposite surface of the substrate with silver paste.

Transport measurements were performed using a physical property measurement system (Quantum Design PPMS-9T). Before loading the device, we purged the system several times with dry helium gas (99.999%) at 400 K. The longitudinal resistance and Hall resistance were measured using lock-in amplifiers (Stanford Research 830), with applied current of 5–500 nA. The gate voltage was supplied by a Keithley 2400 source meter and applied at 300 K.

In situ magnetic susceptibility measurements were performed using a SQUID magnetometer (Quantum Design MPMS-5T). The measuring rod was made by ourselves. We have built an electrical measurement module. A Keithley 2400 source meter was used to apply the gate voltage. In order to obtain strong signals, $SrCoO_{2.5}$ thin films with a size of $5 \times 5\,mm^2$ (the size of $Ce_{0.8}Gd_{0.2}O_{1.9}$ thin films is $10 \times 7\,mm^2$) were used for measurements. The $SrCoO_{2.5}$ film was patterned into a standard four-electrode configuration and the resistance was measured by a lock-in amplifier (Stanford Research 830) to monitor the status of the sample tuned by the gate voltage. For each gate voltage, after a period of relaxation ranging from tens of seconds to tens of minutes at 300 K, the sample resistance became saturated, and then the magnetic susceptibility measurement was carried out. A magnetic field of 0.5 T parallel to the plane of the thin film was applied.

X-ray diffraction (XRD) data were collected by an x-ray diffractometer (SmartLab-9, Rikagu Corp.) with Cu $K\alpha$ radiation. For the *in situ* XRD measurements, the device was placed onto a temperature-control holder in the TTK450 Anton Paar chamber. We have built an electrical measurement module. The resistance of the sample was simultaneously monitored during XRD measurements. In order to obtain strong XRD signals, $SrCoO_{2.5}$ thin films with a size of $5 \times 5\,mm^2$ (the size of $Ce_{0.8}Gd_{0.2}O_{1.9}$ thin films is $10 \times 10\,mm^2$) were used for the XRD measurements. The diffraction data were collected at room temperature. For each gate voltage, after a period of

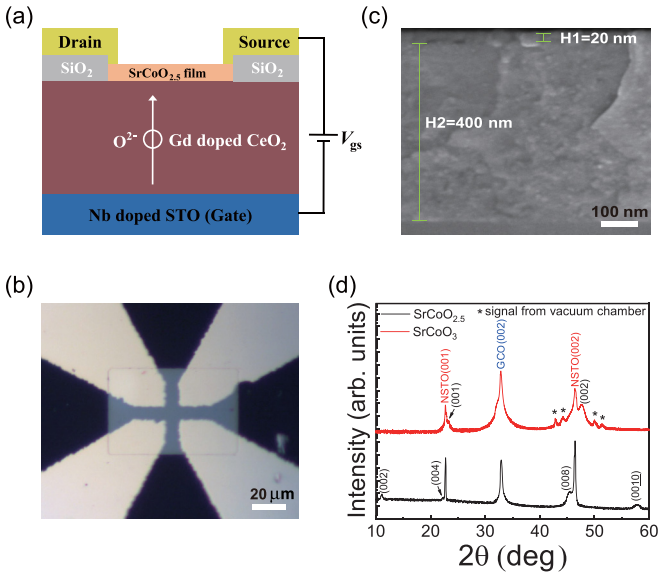

FIG. 1. Fabrication and characterizations of the $SrCoO_{2.5}$ thin film transport device. (a) Schematic illustration of the OICFET device and the electric-field-controlled oxygen migration process. (b) Optical image of a typical $SrCoO_{2.5}$ device with the van der Pauw configuration. Scale bar, 20 μm. (c) Cross-sectional scanning electron microscopy (SEM) images of a $SrCoO_{2.5}$ thin film grown on the Gd-doped CeO_2 film. Scale bar, 100 nm. (d) X-ray diffraction θ-2θ scans of as-grown $SrCoO_{2.5}$ film and oxidized $SrCoO_3$ thin film. The XRD data of the as-grown $SrCoO_{2.5}$ film was first collected, and then the sample was loaded into the TTK450 Anton Paar chamber and was tuned to $SrCoO_3$ by electric-field-controlled oxygen doping. The diffraction peaks marked with a star are from the electrical measurement module built in the vacuum chamber.

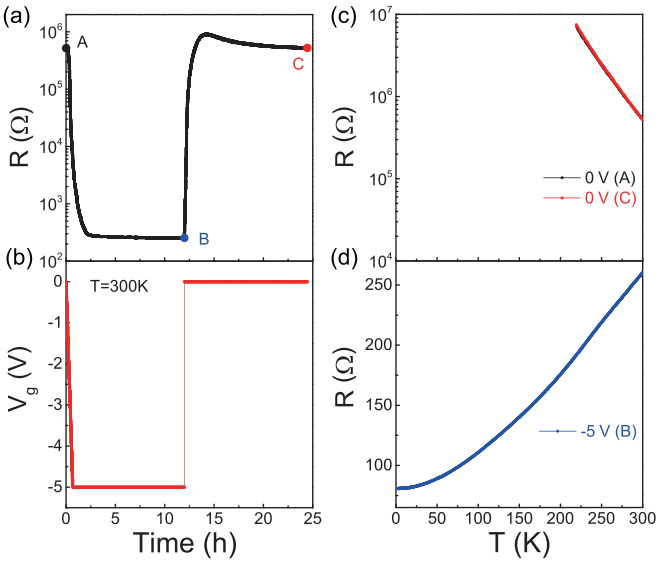

FIG. 2. Electric-field-controlled oxygen migration in the $SrCoO_{2.5+x}$ ($0 \leqslant x \leqslant 0.5$) thin film with thickness of 20 nm. (a) Time-dependent resistance of the $SrCoO_{2.5+x}$ thin film at different gate voltages. (b) Time-dependent gate voltages applied on the device. (c), (d) Temperature dependence of the resistance for the $SrCoO_{2.5+x}$ thin film at different gate voltages during the gating process.

relaxation ranging from tens of seconds to tens of minutes at 300 K, the sample resistance became saturated, and then the diffraction data were collected. During the experiment, the vacuum of the chamber was kept below 10 Pa.

III. RESULTS AND DISCUSSION

Figure 1(a) depicts a schematic illustration of the OICFET device with as-grown $SrCoO_{2.5}$ thin film as the transport channel, and Fig. 1(b) shows an optical image of a typical $SrCoO_{2.5}$ device with the van der Pauw configuration. In this study, the typical thicknesses of $SrCoO_{2.5}$ and GCO films are ∼20 and ∼400 nm, respectively, which are determined by scanning electron microscopy (SEM) [Fig. 1(c)]. Gd-doped CeO_2 is chosen as the gate dielectric because of its high oxygen ionic conductivity at relatively low temperature. Due to 20% tetravalent Ce^{4+} being replaced by trivalent Gd^{3+}, about 5% oxygen vacancies are formed to keep the valence balanced in the $Ce_{0.8}Gd_{0.2}O_{1.9}$ film [22]. The migration of oxygen ions through the oxygen vacancies at an applied field provides the migration channel [22]. Because the oxygen vacancies are not ordered, the migration channels have no directionality. It should be emphasized that in our device configuration, the upper surface of the sample is fully exposed, making heterostructure/interface engineering and surface spectroscopic study convenient. Figure 1(d) displays the XRD θ-2θ scans of the as-grown $SrCoO_{2.5}$ thin film (black). Only $(00l)$ peaks are observed in the scans, and the x-ray rocking-curve analysis of the (002) peak (see Fig. S1(b) in the Supplemental Material [23]) reveals a full width at half maximum (FWHM) ∼0.07°, indicating that the as-grown $SrCoO_{2.5}$ films are of excellent crystalline quality, which benefits from the extremely flat surface of the GCO film (see Fig. S2 in the Supplemental Material [23]). In brownmillerite $SrCoO_{2.5}$, the long-range order of oxygen vacancies gives rise to a distinct superstructure with alternate stacking of octahedral CoO_6 and tetrahedral CoO_4 layers along the c direction [24,25]. The one-dimensional oxygen vacancy channels within CoO_4 layers usually lead to high ionic conductivity; they are parallel to the thin film surface and along the [1–10] direction [25]. The c-axis lattice parameter of our as-grown $SrCoO_{2.5}$ film calculated from the XRD data is 16.0058 Å, slightly larger than the bulk lattice parameter of $c = 15.7450$ Å [24]. This difference is likely due to the in-plane compressive strain introduced by the GCO layer. The lattice parameter of the ∼400 nm GCO film calculated from the XRD data is $a = 5.3978$ Å, which corresponds to $a/\sqrt{2} = 3.8168$Å, whereas the bulk $SrCoO_{2.5}$ has a larger pseudotetragonal lattice parameter of $a_t = 3.905$ Å [12,14]. The cross-sectional STEM measurement confirms the existence of 1.3% compressive stress (see Fig. S3 in the Supplemental Material [23]). It should be pointed out that the lattice parameter of the bulk $Ce_{0.8}Gd_{0.2}O_{1.9}$ is $a = 5.3987$ Å, suggesting that the ∼400 nm GCO film is completely relaxed.

As shown in Fig. 2(c), the as-grown $SrCoO_{2.5}$ thin film with a thickness of 20 nm exhibits a strong insulating behavior above 220 K and the resistance exceeds the measurable range of our experimental setup at lower temperatures, consistent

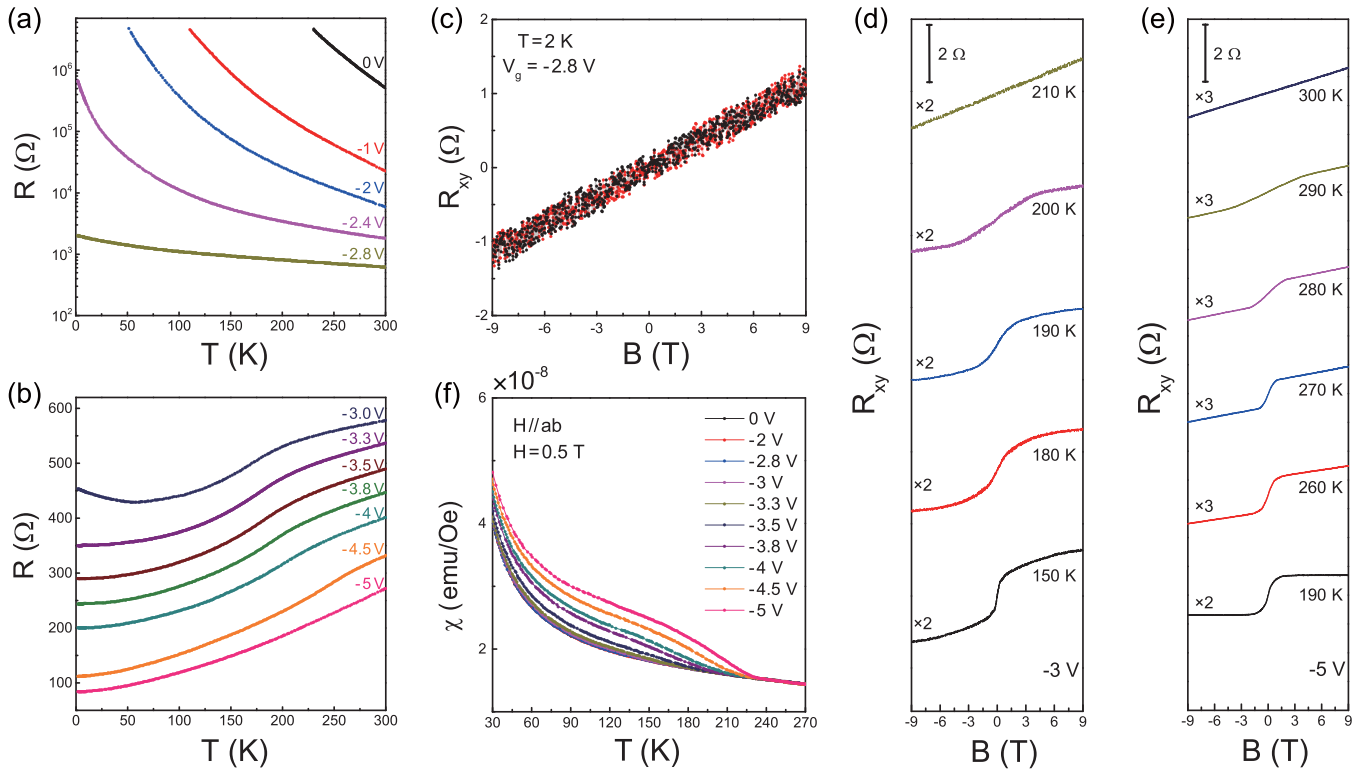

FIG. 3. Temperature-dependent resistance, Hall resistance [$R_{xy}(B)$] and *in situ* magnetic susceptibility measurements for $SrCoO_{2.5+x}$ ($0 \leqslant x \leqslant 0.5$) thin film with thickness of 20 nm at different gate voltages. (a) Temperature dependence of resistance at the gate voltages from 0 to −2.8 V. (b) Temperature dependence of resistance at the gate voltages from −3 to −5 V. (c)–(e) Temperature dependence of $R_{xy}(B)$ at representative gate voltages. The $R_{xy}(B)$ curves are shifted vertically for clarity. (f) *In situ* magnetic susceptibility measurements for $SrCoO_{2.5+x}$ ($0 \leqslant x \leqslant 0.5$) thin film with a thickness of 20 nm and a size of $5 \times 5\,mm^2$ at different gate voltages. All the measurements are done by applying a magnetic field of 0.5 T parallel to the plane of the film in the zero-field-cooled conditions.

with previous reports [9,11,12,16,26,27]. Then we apply gate voltages on the sample and test the oxygen-modulation ability for this recently developed OICFET device. First, a gate voltage of −5 V was applied and kept on for about 12 h at 300 K. The negative gate voltage will drive the oxygen ions in the GCO film to accumulate at the GCO/SCO interface and then enter into the SCO film to fill the oxygen vacancies. At the beginning, the oxygen concentration near the interface is higher. During the relaxation process, oxygen ions will diffuse along both the in-plane and out of plane directions of the sample. As a result, the resistance of the sample instantly decreases, and gradually tends to saturate [from A to B in Fig. 2(a)]. When cooling down the device to below 290 K, the oxygen ions in the GCO film are frozen [28] and the oxygen content in the $SrCoO_{2.5+x}$ thin film is fixed (see Fig. S4 in the Supplemental Material [23]). Figure 2(d) shows the temperature-dependent resistance at point B, and typical metallic behavior is observed. With filling of the oxygen vacancies, the brownmillerite phase transforms to the perovskite phase, resulting in an insulator-to-metal transition in $SrCoO_{2.5+x}$. The temperature was swept back to 300 K, and then the gate voltage was switched off and kept at zero for about 12 h. As shown in Fig. 2(a), the resistance of the sample increases rapidly and then tends to saturate (from B to C). An insulating state recovers and the *R-T* curve nearly overlaps with what is measured in the as-grown $SrCoO_{2.5}$ thin film [red curve in Fig. 2(c)]. These results suggest that the electric field control of oxygen concentration dominates the transport properties of $SrCoO_{2.5+x}$ during the gating process in the OICFET device. The reversible phase transition is achieved by making the gate voltage zero, indicating a volatile phase transition, which is in contrast to previous results [16]. It is known that the strained perovskite $SrCoO_{3-\delta}$ can be stable for a few days or months [29]; however, in this work the rate with which it is back to $SrCoO_{2.5}$ is rather fast after the release of the gate voltage. The high-quality epitaxial interface between the $SrCoO_{2.5+x}$ film and the GCO film (see Fig. S3 in the Supplemental Material [23]) as well as the existence of the oxygen migrating channel in the GCO film [22] is beneficial to the migration of oxygen ions. Additionally, the compressive strain may facilitate oxygen migration by reducing the energy barrier for oxygen migration [30]. Importantly, these two phases can be reversibly switched at room temperature (see Fig. S5 in the Supplemental Material [23]), a remarkably reduced temperature compared to previous results [11,12,14], which is attributed to the significantly reduced Gibbs free-energy difference between the two topotatic phases at low temperature [11]. The excellent reversibility is an intrinsic property of our gating technology, which is likely to be closely linked to the oxygen vacancies in GCO [28]. It should be pointed out that the room-temperature resistance changes as much as about four orders of magnitude. Reversible

change between a high-resistance state and a low-resistance state shows a resistance-switching phenomenon, which has been widely observed in many transition-metal-oxide materials [26].

In order to further understand the reversible transition from an insulating state to a metallic state in the $SrCoO_{2.5+x}$ film driven by electric-field-controlled oxygen migration, we carried out a systematic study to track the evolution of the electronic, magnetic, and structural properties in this system. In order to achieve fine control of the oxygen concentration, we start with a small gate voltage at 300 K, and then slowly increase the voltage after the sample resistance becomes saturated. For each gate voltage, the relaxation times range from tens of seconds to tens of minutes; they strongly depend on the applied voltage and the voltage interval. Once a target resistance is reached, we cool down the device and perform temperature-dependent resistance measurements. The fine-tuning process enables us to continuously tune the oxygen concentration and track the evolution of the electronic state from the insulating state all the way to the metallic state in a single device. In order to improve the homogeneity of oxygen doping, we selected the $SrCoO_{2.5}$ thin film with a thickness of 20 nm for the transport measurements. Figures. 3(a) and 3(b) display the temperature-dependent resistance of a $SrCoO_{2.5+x}$ thin film with a thickness of 20 nm at the gate voltages from 0 to −5 V. Initially, the as-grown brownmillerite $SrCoO_{2.5}$ film exhibits a strong insulating behavior. The negative gate voltages drive oxygen ions into the sample to gradually fill the oxygen vacancies, leading to a progressive decrease of the sample resistance as well as the suppression of the insulating behavior. The room-temperature resistance decreases by nearly four orders of magnitude from about 500 to about 0.25 kΩ. At $V_g < -3$ V, the sample shows insulating behavior in the whole temperature range (2–300 K), while the sample becomes metallic at $V_g > -3$ V. At $V_g = -3$ V, the up-turn feature in the resistance at low temperatures arises from the coexistence of the brownmillerite phase and the perovskite phase confirmed by x-ray diffraction results. The *R-T* curves from −3 to −5 V show an obvious slope change at high temperature. The derivatives of these *R-T* curves are shown in Fig. S6 (see the Supplemental Material [23]). We observe an obvious peak in each derivative curve. Furthermore, the temperature corresponding to the peak increases with the increase of gate voltage, which may be a signature of the ferromagnetic transition.

Ferromagnetic materials spontaneously break time-reversal symmetry and can host a transverse Hall field even in the absence of a magnetic field, giving rise to the anomalous Hall effect (AHE) [31]. In a ferromagnetic state, the total Hall resistance R_{xy} can be expressed as $R_{xy} = R_A M + R_H H$, where R_A and R_H are the anomalous and ordinary Hall coefficients, respectively [32]. The anomalous Hall effect has been observed in the perovskite $SrCoO_3$ [33,34]. Interestingly, the electric-field-controlled phase transformation is also accompanied by a change of magnetic properties in the $SrCoO_{2.5+x}$ thin film. To further reveal the evolution of magnetic properties during the gating process, temperature-dependent $R_{xy}(B)$ is measured at different gate voltages. It should be pointed out that the Hall signal cannot be detected due to the strong insulating behavior in the as-grown $SrCoO_{2.5}$ film. Oxygen content (x) in the $SrCoO_{2.5+x}$-based device is continuously modulated by the gate voltages; consequently we can control their magnetic properties. As shown in Fig. 3(c), at $V_g = -2.8$ V, $R_{xy}(B)$ shows linear behavior at 2 K, indicating the sample is still in the antiferromagnetic state. However, when the gate voltage reaches −3 V, an anomalous Hall term appears below 210 K as shown in Fig. 3(d), indicating a ferromagnetic ground state. As shown in Fig. 3(e) and Fig. S7 (see the Supplemental Material [23]), the anomalous Hall signature persists to higher temperature with further increasing the gate voltage, indicating that the Curie temperature is enhanced by the increase of the oxygen content.

In general, the temperature at which the anomalous Hall effect disappears should be higher than the Curie temperature (T_C) due to the presence of spin fluctuations. In order to determine the Curie temperature, we performed *in situ* magnetic susceptibility measurements for the $SrCoO_{2.5+x}$ thin film with a thickness of 20 nm and a size of $5 \times 5\,mm^2$ at different gate voltages. The size of the GCO film is $10 \times 7\,mm^2$, which is much larger than that of the $SrCoO_{2.5}$ thin film, ensuring the homogeneity of the tuning process. Figure 3(f) shows the evolution of the magnetic susceptibility χ as a function of temperature at different gate voltages. All the measurements are carried out by applying a magnetic field of 0.5 T parallel to the *ab* plane of the film in the zero-field-cooled conditions. It should be addressed that the Gd-doped CeO_2 film is paramagnetic, which may prohibit the direct magnetic measurement of the SCO film grown on it. However, the magnetic susceptibility $\Delta\chi[\Delta\chi = \chi(V_g) - \chi(0\,V)]$ can still reflect the magnetic properties of the SCO film. The χ-T curve for the as-grown $SrCoO_{2.5}$ film (see Fig. S8(a) in the Supplemental Material [23]) shows clear Curie-Weiss behavior. In contrast, the oxidized $SrCoO_3$ thin film ($V_g = -5$ V) (see Fig. S9 in the Supplemental Material [23]) shows a clear magnetic transition at ∼235 K. A hysteresis loop is observed at 5 K (see the inset of Fig. S8(a) in the Supplemental Material [23]), confirming the ferromagnetic nature of $SrCoO_3$. The saturation magnetization value in Bohr magnetons per cobalt at 5 K is about $0.3\,\mu_B$ (see Fig. S10 in the Supplemental Material [23]), which is lower than that of bulk $SrCoO_3$ ($\sim 2.5\,\mu_B$) [35] and $SrCoO_3$ film grown on the $(La, Sr)(Al, Ta)O_3$ substrate ($\sim 1.4\,\mu_B$) [13]. Owing to the weak magnetic signal, the quantitative analysis of *in situ* magnetic susceptibility data may be wildly inaccurate. The ferromagnetic transition temperature is consistent with the previously reported value in high-quality $SrCoO_3$ films grown on LSAT [13], but lower than that of bulk $SrCoO_3$ ($T_C \sim 280$–305 K) [35,36], which may be caused by in-plane compressive stress. As shown in Fig. 3(f) and Fig. S8(b) in the Supplemental Material [23], the χ-T curves nearly overlap with each other at gate voltages ranging from 0 to −2.8 V, and a magnetic transition at ∼147 K is first observed at $V_g = -3$ V, consistent with the result of Hall measurements. In addition, T_C ∼147 K is close to the value observed in the previously identified perovskite $SrCoO_{2.75}$ phase [36]. The details for determining the magnetic transition temperature are shown in Fig. S8(b) (see the Supplemental Material [23]). It should be addressed

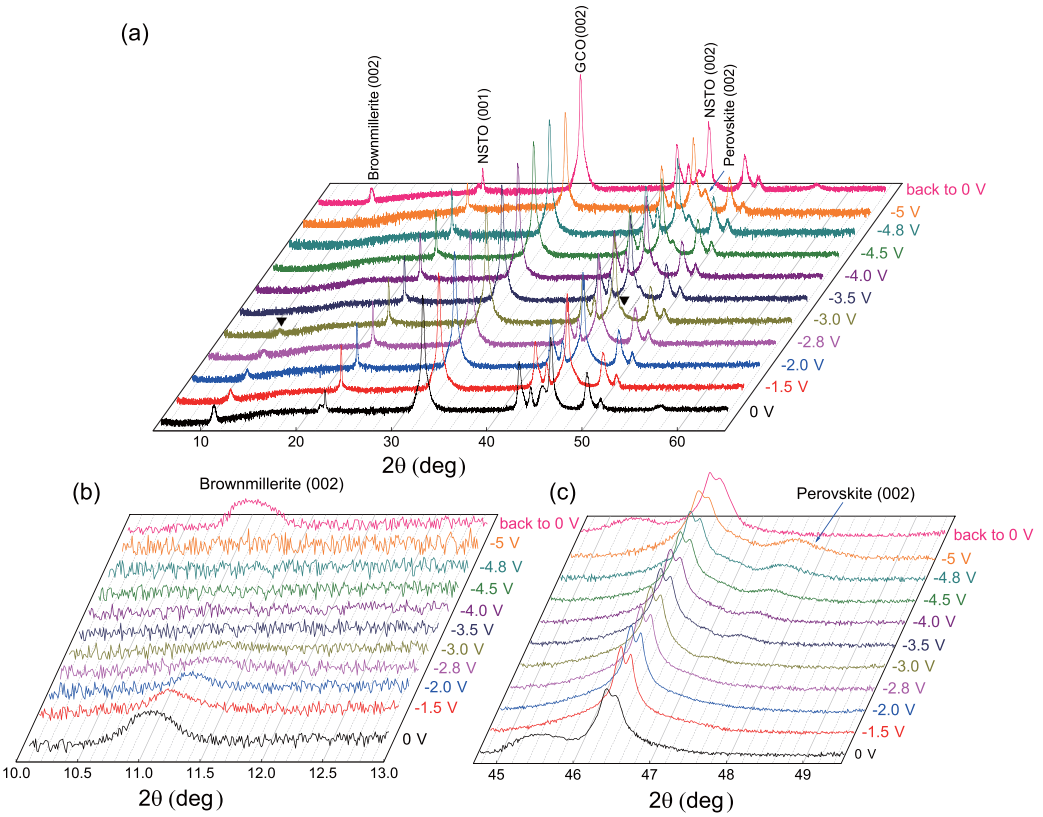

FIG. 4. *In situ* x-ray diffraction patterns of the $SrCoO_{2.5+x}$ ($0 \leqslant x \leqslant 0.5$) thin film with a thickness of 20 nm and a size of $5 \times 5\,mm^2$ at various gate voltages. (a) The XRD pattern evolution of the $SrCoO_{2.5+x}$ ($0 \leqslant x \leqslant 0.5$) thin film during the gating process. The "▼" symbol shows the coexistence of the brownmillerite phase and the perovskite phase. (b) The evolution of the (002) diffraction peak of the brownmillerite phase at various gate voltages. (c) The evolution of the (002) diffraction peak of the perovskite phase at various gate voltages.

that we do not observe two magnetic transitions widely observed in the bulk chemically oxidized $SrCoO_{2.5+x}$ due to the inhomogeneity of oxygen content [36,37], suggesting the uniformity of electric-field-controlled phase transformation in our device.

To track the structural evolution during the gating process, we performed *in situ* XRD measurements at different gate voltages. The diffraction data were collected at room temperature. In order to improve the homogeneity of oxygen doping, we selected the $SrCoO_{2.5}$ thin film with a thickness of 20 nm and a size of $5 \times 5\,mm^2$ for the *in situ* XRD measurements. Figure 4(a) illustrates the structural evolution of the $SrCoO_{2.5+x}$ ($0 \leqslant x \leqslant 0.5$) thin film during the gating process. The collapse of the brownmillerite phase and the emergence of the perovskite phase can be clearly observed. Two diffraction peaks, namely, the brownmillerite phase (002) and the perovskite phase (002) peaks, are highlighted to track the phase transformation in Figs. 4(b) and 4(c), respectively. The brownmillerite (002) peak, located at $2\theta = 11.05^\circ$, is a unique "fingerprint" for the presence of the brownmillerite phase, which originates from the superstructure of oxygen vacancies [14]. With increasing the gate voltage, the intensity of the original (002) peak gradually diminishes and its position shifts to a higher angle. When the gate voltage reaches −3.5 V, this peak completely disappears, while the (002) peak at 47.23° for the perovskite phase clearly shows up at $V_g = -3$ V, and the (002) peak of the perovskite phase becomes strong and shifts to a higher angle with further increasing the gate voltage. These results confirm that oxygen ions are driven into the $SrCoO_{2.5}$ thin film and fill the oxygen vacancies, leading to a structural transformation from the brownmillerite $SrCoO_{2.5}$ to the perovskite $SrCoO_3$. When the gate voltage is switched off and kept at zero for about 12 h, the perovskite $SrCoO_3$ completely reverts to the brownmillerite $SrCoO_{2.5}$. It should be pointed out that the location of the GCO peaks does not change with gate voltages, suggesting that the lattice parameters are unchanged for GCO film when oxygen ions are driven in and out with V_g. By the Gaussian peak fitting, the Scherrer lengths (Λ) of the (002) diffraction peaks of the brownmillerite phase and the perovskite phase were extracted (see Fig. S11 of the Supplemental Material [23]). The Scherrer length gradually decreases with increasing the gate voltage, indicating that the sample gradually becomes inhomogeneous. Furthermore, the Scherrer lengths of the perovskite phase are distinctly lower than that of the brownmillerite phase, meaning that the perovskite phase has lesser through-plane structural coherence, likely indicating that the brownmillerite-perovskite transformation is inhomogeneous across the thickness of the SCO film. At $V_g = -3$ V, the trace of the brownmillerite (002) peak is still observed, which indicates the coexistence of the brownmillerite phase and the perovskite phase, arising from the inhomogeneous

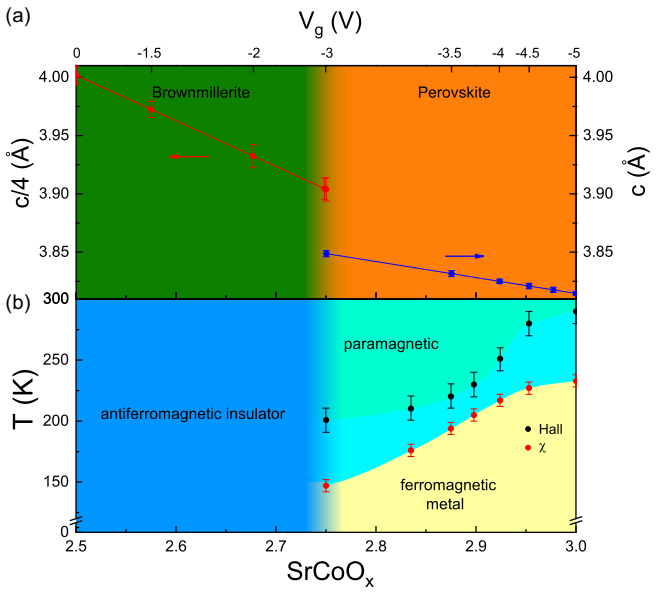

FIG. 5. The phase diagram of the gate-tuned $SrCoO_{2.5+x}$ ($0 \leqslant x \leqslant 0.5$) thin film. (a) The c-axis lattice parameter as a function of gate voltage and oxygen content for the $SrCoO_{2.5+x}$ ($0 \leqslant x \leqslant 0.5$) thin film. The c-axis lattice parameter is determined by the position of the (002) diffraction peaks of the brownmillerite phase and the perovskite phase from the *in situ* XRD measurements. (b) The phase diagram of the gate-tuned $SrCoO_{2.5+x}$ ($0 \leqslant x \leqslant 0.5$) thin film from the antiferromagnetic insulator to the ferromagnetic metal. The ferromagnetic transition temperatures (T_C) at different gate voltages are determined by the *in situ* magnetic susceptibility measurements and the Hall measurements, respectively.

distribution of oxygen ions. The sample is in the brownmillerite phase and the perovskite phase for $-3\,\mathrm{V} < V_g \leqslant 0\,\mathrm{V}$ and $-5\,\mathrm{V} \leqslant V_g < -3\,\mathrm{V}$, respectively. Such an inhomogeneity strongly depends on the thickness of the $SrCoO_{2.5}$ thin film, which was confirmed by the transport measurements shown in Fig. S12 and *in situ* XRD patterns for the thin film with 30 nm shown in Fig. S13 (see the Supplemental Material [23]). For a thicker $SrCoO_{2.5}$ thin film (30 nm), the coexistence of brownmillerite and perovskite phases has been observed at gate voltages from -3 to -3.8 V. Meanwhile, the sample shows a crossover behavior from an insulating state to a metallic state in the same gate voltage range. When the electric field drives the oxygen ions in the GCO film to enter the SCO film, oxygen ions will diffuse along both the in-plane and out of plane directions of the sample. Due to the oxygen vacancy channels in the plane, oxygen ion diffusion will be faster in the in-plane direction, resulting in a better lateral homogeneity.

Based on the transport, *in situ* susceptibility, and *in situ* x-ray diffraction measurements, the phase diagram of the gate-voltage-tuned $SrCoO_{2.5+x}$ ($0 \leqslant x \leqslant 0.5$) thin film is plotted in Fig. 5. With increasing the gate voltage, oxygen ions are driven into the $SrCoO_{2.5}$ thin film and fill the oxygen vacancies, inducing a structural transformation from the brownmillerite phase to the perovskite phase. The c-axis lattice parameter is determined by the position of (002) diffraction peaks of the brownmillerite phase and the perovskite phase from the *in situ* XRD measurements. The oxygen vacancies in $SrCoO_{2.5+x}$ ($0 \leqslant x \leqslant 0.5$) lead to an expansion of the c-axis lattice parameter. Hence, the lattice parameter of the c axis monotonically decreases with increasing the gate voltage and oxygen content. Although it is usually difficult to determine the oxygen content in oxide materials, we find clues in $SrCoO_{2.5+x}$ ($0 \leqslant x \leqslant 0.5$) that allow us to extract the oxygen concentration. As mentioned above, a magnetic transition at ~147 K was observed for $V_g = -3$ V in magnetic susceptibility measurements, which is close to the Curie temperature in perovskite $SrCoO_{2.75}$ [36]. The c-axis lattice constant for the perovskite structure at $V_g = -3$ V is 3.849 Å, which is nearly the same as the value of 3.842 Å in perovskite $SrCoO_{2.75}$ polycrystalline powder [38]. Moreover, a transformation from polycrystalline $SrCoO_{2.5}$ with brownmillerite structure to an intermediate $SrCoO_{2.75}$ phase with perovskite structure has been reported, using electrochemical oxidation methods [37,39]. Therefore, it is reasonable to assume that the oxygen content is 2.75 at the gate voltage of about -3 V. We noticed that the c-axis lattice parameter of the brownmillerite structure gradually tends to saturate with increasing the gate voltage. For $SrCoO_{2.5+x}$ thin film with thickness of 20 nm, the c-axis lattice parameters at $V_g = -2.8$ V ($0 = 15.6177$ Å) and -3 V ($c = 15.6154$ Å) for the brownmillerite structure are almost the same, as shown in Fig. 5(a). Similar results are also observed at $V_g = -3.5$ V ($c = 15.6172$ Å) and -3.8 V ($c = 15.6163$ Å) for a 30 nm sample (see Fig. S14 in the Supplemental Material [23]). These results suggest that the oxygen content of 2.75 is the limit of the brownmillerite structure. According to Vegard's law, the oxygen doping concentration should depend linearly on the c-axis lattice constant [40–42], and then the oxygen content corresponding to each gate voltage can be obtained. A structural transformation from the brownmillerite $SrCoO_{2.5}$ to the perovskite $SrCoO_3$ is accompanied by a magnetic phase transition from an antiferromagnetic state to a ferromagnetic state, as shown in Fig. 5(b). The gate voltage of -3 V separates the brownmillerite structure with insulating antiferromagnetism and the perovskite structure with metallic ferromagnetism. The Curie temperatures at different gate voltages are determined by the *in situ* magnetic susceptibility measurements and the Hall measurements, respectively. With increasing the gate voltage from -3 to -5 V, the oxygen vacancies in the perovskite $SrCoO_{3-\delta}$ are gradually filled by electric-field-controlled oxygen migration, resulting in the increase of the Curie temperature. The in-plane lattice parameter of the oxidized $SrCoO_3$ thin film ($V_g = -5$ V) calculated from the XRD data is 3.8149 Å, providing compressive strain (0.37%) with respect to the lattice constant (3.829 Å) of bulk $SrCoO_3$ [35], which may result in a lower T_C than that of bulk $SrCoO_3$ [35,36]. Although the topotactic transformation of $SrCoO_{2.5+x}$ has been realized in previous experiments [11,12,14,16,19,20], adopting Gd-doped CeO_2 as the dielectric layer in a FET device to induce this reversible brownmillerite-perovskite transition at room temperature is also a great advance. Previous studies mainly focused on the two ends of the phase transition, and paid little attention to the intermediate process. However, in this work the fine-tuning process enables us to continuously tune the oxygen concentration

in a single device and map out a comprehensive phase diagram of the $SrCoO_{2.5+x}$ ($0 \leqslant x \leqslant 0.5$) thin film from an antiferromagnetic insulator all the way to a ferromagnetic metal.

IV. CONCLUSION

In conclusion, using our recently developed OICFET device, we successfully achieve a reversible phase transformation between brownmillerite $SrCoO_{2.5}$ and perovskite $SrCoO_3$ driven by electric-field-controlled oxygen migration at room temperature, and carry out a systematic study to track the evolution of the electronic, magnetic, and structural properties in the $SrCoO_{2.5+x}$ system. With continuously changing the oxygen content, a comprehensive phase diagram of the $SrCoO_{2.5+x}$ ($0 \leqslant x \leqslant 0.5$) thin film from an antiferromagnetic insulator to a ferromagnetic metal is mapped out in a single device. Our results establish the OICFET device as a powerful tool to continuously and reversibly modulate oxygen content in oxide materials, which has great potential to explore unique physical properties and modulate the physical states, and to serve as the next generation all-solid-state FET.

ACKNOWLEDGMENTS

This work was supported by the National Natural Science Foundation of China (Grants No. 11888101, No. 11534010, and No. 12004365), the National Key Research and Development Program of the Ministry of Science and Technology of China (Grant No. 2017YFA0303001), the Strategic Priority Research Program of the Chinese Academy of Sciences (Grant No. XDB25000000), the Anhui Initiative in Quantum Information Technologies (Grant No. AHY160000), the Science Challenge Project of China (Grant No. TZ2016004), the Key Research Program of Frontier Sciences, CAS, China (Grant No. QYZDYSSW-SLH021), and the National Postdoctoral Program for Innovative Talents (Grant No. BX20190319).

[1] J. G. Bednorz and K. Müller, Z. Phys. B **64**, 189 (1986).
[2] C. H. Ahn, A. Bhattacharya, M. Di Ventra, J. N. Eckstein, C. D. Frisbie, M. E. Gershenson, A. M. Goldman, I. H. Inoue, J. Mannhart, A. J. Millis, A. F. Morpurgo, D. Natelson, and J.-M. Triscone, Rev. Mod. Phys. **78**, 1185 (2006).
[3] J.-H. Park, E. Vescovo, H.-J. Kim, C. Kwon, R. Ramesh, and T. Venkatesan, Nature (London) **392**, 794 (1998).
[4] F. Trier, G. E. D. K. Prawiroatmodjo, Z. Zhong, D. V. Christensen, M. von Soosten, A. Bhowmik, J. M. G. Lastra, Y. Chen, T. S. Jespersen, and N. Pryds, Phys. Rev. Lett. **117**, 096804 (2016).
[5] Y. Tokura, Y. Taguchi, Y. Okada, Y. Fujishima, T. Arima, K. Kumagai, and Y. Iye, Phys. Rev. Lett. **70**, 2126 (1993).
[6] S. V. Kalinin and N. A. Spaldin, Science **341**, 858 (2013).
[7] B. O. Wells, Y. S. Lee, M. A. Kastner, R. J. Christianson, R. J. Birgeneau, K. Yamada, Y. Endoh, and G. Shirane, Science **277**, 1067 (1997).
[8] K. Semba and A. Matsuda, Phys. Rev. Lett. **86**, 496 (2001).
[9] N. Ichikawa, M. Iwanowska, M. Kawai, C. Calers, W. Paulus, and Y. Shimakawa, Dalton Trans. **41**, 10507 (2012).
[10] Y. J. Yu, L. G. Ma, P. Cai, R. D. Zhong, C. Ye, J. Shen, G. D. Gu, X. H. Chen, and Y. B. Zhang, Nature (London) **575**, 156 (2019).
[11] H. Jeen, W. S. Choi, M. D. Biegalski, C. M. Folkman, I-C. Tung, D. D. Fong, J. W. Freeland, D. Shin, H. Ohta, M. F. Chisholm, and H. N. Lee, Nat. Mater. **12**, 1057 (2013).
[12] H. Jeen, W. S. Choi, J. W. Freeland, H. Ohta, C. U. Jung, and H. N. Lee, Adv. Mater. **25**, 3651 (2013).
[13] Y. J. Wang, Q. He, W. M. Ming, M. H. Du, N. P. Lu, C. Cafolla, J. Fujioka, Q. H. Zhang, D. Zhang, S. C. Shen, Y. Lyu, A. T. N'Diaye, E. Arenholz, L. Gu, C. W. Nan, Y. Tokura, S. Okamoto, and P. Yu, Phys. Rev. X **10**, 021030 (2020).
[14] Q. Y. Lu and B. Yildiz, Nano Lett. **16**, 1186 (2016).
[15] J. Jeong, N. Aetukuri, T. Graf, T. D. Schladt, M. G. Samant, and S. S. P. Parkin, Science **339**, 1402 (2013).
[16] N. P. Lu, P. F. Zhang, Q. H. Zhang, R. M. Qiao, Q. He, H. B. Li, Y. J. Wang, J. W. Guo, D. Zhang, Z. Duan, Z. L. Li, M. Wang, S. Z. Yang, M. Z. Yan, E. Arenholz, S. Y. Zhou, W. L. Yang, L. Gu, C. W. Nan *et al.*, Nature (London) **546**, 124 (2017).
[17] H. Y. Huang, C. Ge, Q. H. Zhang, C. X. Liu, J. Y. Du, J. K. Li, C. Wang, L. Gu, G. Z. Yang, and K. J. Jin, Adv. Funct. Mater. **29**, 1902702 (2019).
[18] U. Bauer, S. Emori, and G. S. D. Beach, Nat. Nanotechnol. **8**, 411 (2013).
[19] T. Katase, Y. Suzuki, and H. Ohta, Adv. Electron. Mater. **2**, 1600044 (2016).
[20] D. Wang, L. P. Meng, L. Wei, P. Shi, Y. X. Chen, S. S. Yan, Y. F. Tian, G. L. Liu, and L. M. Mei, J. Magn. Magn. Mater. **496**, 165926 (2020).
[21] V. Chaturvedi, W. M. Postiglione, R. D. Chakraborty, B. Q. Yu, W. Tabiś, S. Hameed, N. Biniskos, A. Jacobson, Z. Zhang, H. Zhou, M. Greven, V. E. Ferry, and C. Leighton, ACS Appl. Mater. Interfaces **13**, 51205 (2021).
[22] A. Tsoga, A. Naoumidis, and D. Stöver, Solid State Ionics **135**, 403 (2000).
[23] See Supplemental Material at http://link.aps.org/supplemental/10.1103/PhysRevMaterials.7.044002 for more details about structural characterizations of as-grown $SrCoO_{2.5}$ thin film, temperature-dependent Hall resistance $R_{xy}(B)$, and *in situ* magnetic susceptibility measurements for $SrCoO_{2.5+x}$ ($0 \leqslant x \leqslant 0.5$) thin film with thickness of 20 nm at different gate voltages; and temperature-dependent resistance, *in situ* x-ray diffraction measurements, and *c*-axis lattice parameter for $SrCoO_{2.5+x}$ ($0 \leqslant x \leqslant 0.5$) thin films with thickness of 30 nm at different gate voltages.
[24] A. Muñoz, C. de la Calle, J. A. Alonso, P. M. Botta, V. Pardo, D. Baldomir, and J. Rivas, Phys. Rev. B **78**, 054404 (2008).
[25] J. H. Song, Y. S. Chen, H. R. Zhang, F. R. Han, J. Zhang, X. B. Chen, H. L. Huang, J. Zhang, H. Zhang, X. Yan, T. Khan, S. J. Qi, Z. H. Yang, F. X. Hu, B. G. Shen, and J. R. Sun, Phys. Rev. Mater. **3**, 045801 (2019).

[26] O. T. Tambunan, K. J. Parwanta, S. K. Acharya, B. W. Lee, C. U. Jung, Y. S. Kim, B. H. Park, H. Jeong, J. Y. Park, M. R. Cho, Y. D. Park, W. S. Choi, D. W. Kim, H. Jin, S. Lee, S. J. Song, S. J. Kang, M. Kim, and C. S. Hwang, Appl. Phys. Lett. **105**, 063507 (2014).

[27] J. R. Petrie, C. Mitra, H. Jeen, W. S. Choi, T. L. Meyer, F. A. Reboredo, J. W. Freeland, G. Eres, and H. N. Lee, Adv. Funct. Mater. **26**, 1564 (2016).

[28] B. Lei, D. H. Ma, S. H. Liu, Z. L. Sun, M. Z. Shi, W. Z. Zhuo, F. H. Yu, G. D. Gu, Z. Y. Wang, and X. H. Chen, Natl. Sci. Rev. **9**, nwac089 (2022).

[29] S. Chowdhury, R. J. Choudhary, and D. M. Phase, ACS Appl. Electron. Mater. **3**, 5095 (2021).

[30] Z. Yin, J. L. Wang, J. Wang, J. Li, H. B. Zhou, C. Zhang, H. Zhang, J. Zhang, F. R. Shen, J. Z. Hao, Z. B. Yu, Y. H. Gao, Y. X. Wang, Y. Z. Chen, J. R. Sun, X. D. Bai, J. T. Wang, F. X. Hu, T. Y. Zhao, and B. G. Shen, ACS Nano **16**, 14632 (2022).

[31] N. Nagaosa, J. Sinova, S. Onoda, A. H. MacDonald, and N. P. Ong, Rev. Mod. Phys. **82**, 1539 (2010).

[32] Z. C. Zhang, X. Feng, M. H. Guo, K. Li, J. S. Zhang, Y. B. Ou, Y. Feng, L. L. Wang, X. Chen, K. He, X. C. Ma, Q. K. Xue, and Y. Y. Wang, Nat. Commun. **5**, 4915 (2014).

[33] D. Zhang, H. Ishizuka, N. P. Lu, Y. J. Wang, N. Nagaosa, P. Yu, and Q.-K. Xue, Phys. Rev. B **97**, 184433 (2018).

[34] D. Zhang, Y. J. Wang, N. P. Lu, X. L. Sui, Y. Xu, P. Yu, and Q.-K. Xue, Phys. Rev. B **100**, 060403(R) (2019).

[35] Y. W. Long, Y. Kaneko, S. Ishiwata, Y. Taguchi, and Y. Tokura, J. Phys.: Condens. Matter **23**, 245601 (2011).

[36] C. K. Xie, Y. F. Nie, B. O. Wells, J. I. Budnick, W. A. Hines, and B. Dabrowski, Appl. Phys. Lett. **99**, 052503 (2011).

[37] Z. H. Zhu, F. J. Rueckert, J. I. Budnick, W. A. Hines, Ch. Niedermayer, L. Keller, H. Luetkens, B. Dabrowski, S. Kolesnik, and B. O. Wells, Phys. Rev. B **93**, 224412 (2016).

[38] R. L. Toquin, W. Paulus, A. Cousson, C. Prestipino, and C. Lamberti, J. Am. Chem. Soc. **128**, 13161 (2006).

[39] A. Nemudry, P. Rudolf, and R. Schöllhorn, Chem. Mater. **8**, 2232 (1996).

[40] Ch. Krüger, K. Conder, H. Schwer, and E. Kaldis, J. Solid State Chem. **134**, 356 (1997).

[41] G. Wu, H. X. Yang, L. Zhao, X. G. Luo, T. Wu, G. Y. Wang, and X. H. Chen, Phys. Rev. B **76**, 024513 (2007).

[42] A. F. Wang, J. J. Lin, P. Cheng, G. J. Ye, F. Chen, J. Q. Ma, X. F. Lu, B. Lei, X. G. Luo, and X. H. Chen, Phys. Rev. B **88**, 094516 (2013).